In situ study on radiation response of tungsten manufactured by laser powder bed fusion

Yinghang Liu[a], Tanner O McElroy[a], Chang Xia[a], Adil Wazeer[a], Yexiang Xue[b], Guang Lin[c], Tim Graening[d], Xiao-Ying Yu[d], Wei-ying Chen[e], Haiyan Wang[a,f], and Xinghang Zhang[a*]

[a] *School of Materials Engineering, Purdue University, West Lafayette, IN 47906, United States*

[b]*Department of Computer Science, Purdue University, West Lafayette, IN 47907, USA*

[c]*Department of Mathematics & School of Mechanical Engineering, Purdue University, West Lafayette, IN 47907, USA*

[d]*Materials Science and Technology Division, Oak Ridge National Laboratory, Oak Ridge, TN 37830, USA*

[e]*Nuclear Science and Engineering Division, Argonne National Laboratory, Lemont, IL 60439, USA*

[f]*School of Electrical and Computer Engineering, Purdue University, West Lafayette, IN 47906, United States*

*Corresponding author: Xinghang Zhang, xzhang98@purdue.edu

Abstract:

Tungsten (W) produced by laser powder bed fusion (LPBF) was examined by *in situ* Krypton (Kr) ion irradiation at 400 °C up to 2.52 displacements per atom (dpa) to investigate its radiation response. Dislocation loops with identical Burgers vectors form aligned raft structures, inducing significant grain misorientation accumulation. Defect saturation was observed beyond

0.36 dpa, marked by constant loop density and raft spacing. WO_3 nanoparticles are found in the as-printed matrix and served as efficient defect sinks. Dislocation loops were absorbed at the W/WO_3 interface, facilitating defect annihilation and suppressing defect accumulation. These findings highlight the role of LPBF microstructure and oxide interfaces in mediating radiation-induced defect evolution, offering insights for designing radiation tolerant W-based materials.

Key words: Tungsten (W), laser powder bed fusion (LPBF), *in situ* irradiation, dislocation loop rafts, defect sink.

1. Introduction

Tungsten (W) is considered a primary candidate material for plasma facing components (PFCs) in future fusion reactors owing to its exceptional thermal conductivity, high melting point, and low sputtering yield [1-5]. In the harsh fusion environment, W will be subjected to intense fluxes of 14.1 MeV neutrons and 3.5 MeV helium (He) ions, leading to damage levels on the order of hundreds of displacements per atom (dpa) within a 3 - 5 year operational period [6]. These conditions promote the formation of various radiation induced defects, including vacancy and interstitial dislocation loops, He bubbles, and voids, which seriously degrade the mechanical and thermal properties of W-based components [6-8]. Therefore, understanding the fundamental evolution of these defects is critical for predicting the long-term performance and lifetime of W in fusion systems.

Heavy ion irradiation is commonly employed to simulate neutron damage in W considering its ability to produce comparable displacement cascades in a shorter timeframe compared to neutrons [9-11]. In early studies, Häussermann *et al.* [12-14] irradiated W using 20-70 keV Au ions to fluences below 10^{16} ions/m^2 at room temperature, revealing that the dominant defect species at low doses were edge-type vacancy loops with $\frac{1}{2}$<111> Burgers vector. More recently, Yi et al [15-17]. conducted self-ion irradiation experiments and identified the coexistence of both $\frac{1}{2}$<111> and <100> interstitial loops. The reported loop formation behavior was attributed to the Eyre–Bullough mechanism [18], where faulted loops initially nucleate on the closest-packed {110} planes and subsequently rotate their habit plane to {111}, forming pure edge $\frac{1}{2}$<111> loops during the early stage of damage accumulation.

At higher irradiation doses, the microstructural evolution becomes increasingly complex. Under self-ion irradiation up to 1.4×10^{18} ions/m^2 (corresponding to 0.89 dpa), tangled dislocation networks decorated with discrete loops have been reported [19]. Detailed Burgers vector analysis further confirms the coexistence of $\frac{1}{2}$<111> and <001> interstitial loops at doses up to 0.4 dpa at 300 °C, with approximately 75% of the loops possessing $\frac{1}{2}$<111> character [15]. A distinctive feature at these higher doses is the formation of dislocation loop rafts: linear arrays of loops aligned in parallel with one another, which are believed to significantly influence irradiation induced hardening and embrittlement [15, 20-23]. El-Atwani *et al.* [24] studied the rafting mechanism and confirmed the simulation result by Wen *et al.* [22]. The latter showed the raft formation was driven by the rotation and alignment of Burgers vectors within clustered interstitial loops. It is noted that most of these prior studies are based on post-irradiation analysis, where the microscopy analyses were conducted after the irradiation experiments. *In situ* irradiation study in transmission electron microscope (TEM) is relatively scarce for W and W related alloys.

To improve the irradiation tolerance properties in W, various strategies have been explored, including the development of high-entropy alloys, grain refinement, and the introduction of precipitates [25-29]. Among these, introducing precipitates is a widely recognized approach, as phase boundaries have been shown to act as effective defect sinks, thereby mitigating radiation-induced damage [26, 30-33]. For example, Titanium carbide (TiC) dispersoids in bulk W matrix have been shown to reduce dislocation loop density by acting as vacancy sinks [30]. Despite these advances, the specific interaction mechanism between interstitial loops and such dispersoids remains insufficiently explored, representing a critical gap in the mechanistic understanding of loop-precipitate interactions under irradiation.

Most of the prior irradiation studies have focused on bulk W and W-based alloys [34]. Recently, laser powder bed fusion (LPBF) has emerged as a promising additive manufacturing (AM) approach to produce near-net-shape W components [35-37]. LPBF-W often exhibits microstructural defects such as cracks and porosity, which may arise from the vaporization of tungsten oxide (WO_3) during laser melting, given that its vaporization temperature is lower than the melting point of W [38, 39]. Due to the rapid solidification rates inherent to LPBF, residual WO_3 particles may be entrapped within the W matrix. Despite rapid advancements in AM technologies, the radiation tolerance of LPBF-W remains insufficiently explored.

In this study, we investigate the real-time Kr ion irradiation response of LPBF-W under Kr ion irradiation using *in situ* TEM. By tracking dislocation loop dynamics, loop rafting behavior, and loop-precipitate interactions as a function of the dosage in real time, we aim at exploring the fundamental defect generation and annihilation mechanisms in the unique microstructures of LPBF-W (e.g., *in situ* formed WO_3 particles) and evaluate their defect characteristics that favor the designs of radiation-tolerant W. These findings will facilitate the defect engineering design and processing of AM-W as future PFCs.

2. Materials and methods

Pure W cubes with the dimension of $5 \times 5 \times 8$ mm^3 were fabricated using a Nikon-SLM-125HL machine with a laser power of 250 W, scanning speed of 200 mm/s, hatch spacing of 80 μm, and a layer thickness of 20 μm. The transmission electron microscopy (TEM) sample was prepared by Focused Ion Beam equipped on the same Helios G4 Dual Beam microscope and was irradiated in the intermediate voltage electron microscope (IVEM) with a 300 kV electron beam attached to a Tandem accelerator at Argonne National Laboratory to a fluence of 1.4×10^{15} ions/cm^2 with 1 MeV Kr^{++} at 400 °C. Before and after radiation, the sample was examined using a ThermoFisher TALOS 200X microscope operated at 200 kV with a Super-X energy-dispersive X-ray spectroscopy (EDS) system. Electron energy-loss spectroscopy (EELS) was performed using a ThermoFisher Scientific Themis Z double aberration corrected TEM operated at 300 kV.

During the irradiation process, a CCD camera was used to capture video at 15 frames per second. The ion beam was incident at 30° relative to the electron beam and ~ 15° off the foil normal to ensure complete sample exposure. The average dpa values were calculated to be 2.52 dpa using the Stopping Range of Ions in Matter (SRIM) 2008 with this incidence geometry (Kinchin-Pease method with the displacement energy of 90 eV [7]). The simulated depth dependent damage and Kr ion concentration profiles are shown in Fig. S1. The inverse pole figure (IPF) maps for bulk AM W were acquired by electron backscattered diffraction (EBSD) method on a ThermoFisher Scientific Helios G4 Dual Beam scanning electron microscopy (SEM) with the step size of 1 μm. The high resolution IPF maps for TEM specimens were captured using a NanoMegas ASTAR precession electron diffraction system in a ThermoFisher Scientific Talos 200X TEM microscope with a step size of 10 nm.

3. Results and discussion

The EBSD IPF maps of the as-printed W in Fig. 1a and 1b, obtained from the YZ (parallel to the building direction) and XY (perpendicular to the building direction) planes, respectively, reveal elongated columnar grains aligned along the build direction (Z direction), indicating epitaxial grain growth typical in LPBF processing [37]. Fig. 1c and 1d present high-resolution IPF maps of the *in situ* TEM sample acquired using the ASTAR system before and after irradiation. Corresponding STEM images of the red-boxed areas in Fig. 1c and 1d are shown in Fig. 1g and 1h, respectively. Prior to irradiation, the dislocation density is relatively low and those dislocations are produced by residual stresses from the repeated compression-tension cycles due to local thermal inhomogeneity during LPBF solidification [40, 41]. After irradiation, the formation of high-density dislocation loop rafts is evident. These rafts exhibit a spacing of approximately 20 - 70 nm as shown in Fig. 1h. Fig. S2a and S2b show the HAADF and STEM-DF images of the as-printed sample, displaying oxygen-rich nanoparticles (indicated by yellow arrows) that appear dark in HAADF but bright in the STEM-DF mode. The average diameter of the nanoparticles is measured to be 28 ± 6 nm based on statistics from over 20 particles. The sample thickness in this region is determined to be 110 - 115 nm using EELS, as shown in Fig. S3. Assuming all particles are spherical, the volume fraction of the particles is estimated to be 0.13%. The corresponding EDS compositional profile along the yellow line in Fig. S2d is shown in Fig. S2c, suggesting the particle is primarily composed of W and O elements. The high-resolution TEM (HRTEM) image of a nanoparticle embedded in the W matrix is shown in Fig. S4a. The fast Fourier transform (FFT) pattern obtained from the center of the particle (Fig. S4c) matches well with the monoclinic WO_3 structure, confirming that the particle is primarily composed of WO_3. After irradiation, the EDS line scan of the same particle reveals that oxygen content within the particle region decreases, as shown in Fig. S5. This reduction indicates active oxygen outward diffusion into the W matrix during irradiation, potentially leading to the formation of non-stoichiometric or mixed-phase tungsten oxides within a single particle [42, 43].

To quantify local lattice distortion, misorientation angle maps were extracted along the yellow arrows in Fig. 1c and 1d before and after radiation. As shown in Fig. 1e, the accumulated point-to-origin misorientation increases from ~5° in the as-printed (unirradiated) sample (line 1→2) to ~17° in the irradiated sample (line 3→4) over a 1 μm distance. In contrast, the point-to-point misorientation (Fig. 1f) remains below 0.6° in both cases. This result indicates that loop rafts generate gradual, unidirectional lattice distortion, which culminates in significant local misorientations comparable to those near high-angle grain boundaries (GBs) [44]. Grain refinement has recently been observed in nanocrystalline W-Ta-Cr-V-Hf refractory high-entropy alloys subjected to heavy ion irradiation [45], despite grain coarsening being more commonly reported under irradiation due to enhanced GB mobility and diffusive solute transport [46, 47]. The grain refinement has been attributed to defect clustering at sub-grain boundaries that form cell structures, as well as overlapping displacement cascades of similar scale to the initial grain size (~10 nm), which induce localized grain fragmentation [45, 48]. In the present study, we observe the formation of dislocation loop rafts that organize into cellular-like structures (as shown in Fig. 1h), accompanied by lattice orientation gradients. While no new grains are observed, this raft network may represent an incipient stage of radiation-induced grain subdivision, serving as a framework for accommodating irradiation damage and potentially delaying or preventing grain coarsening, thereby helping to preserve structural integrity.

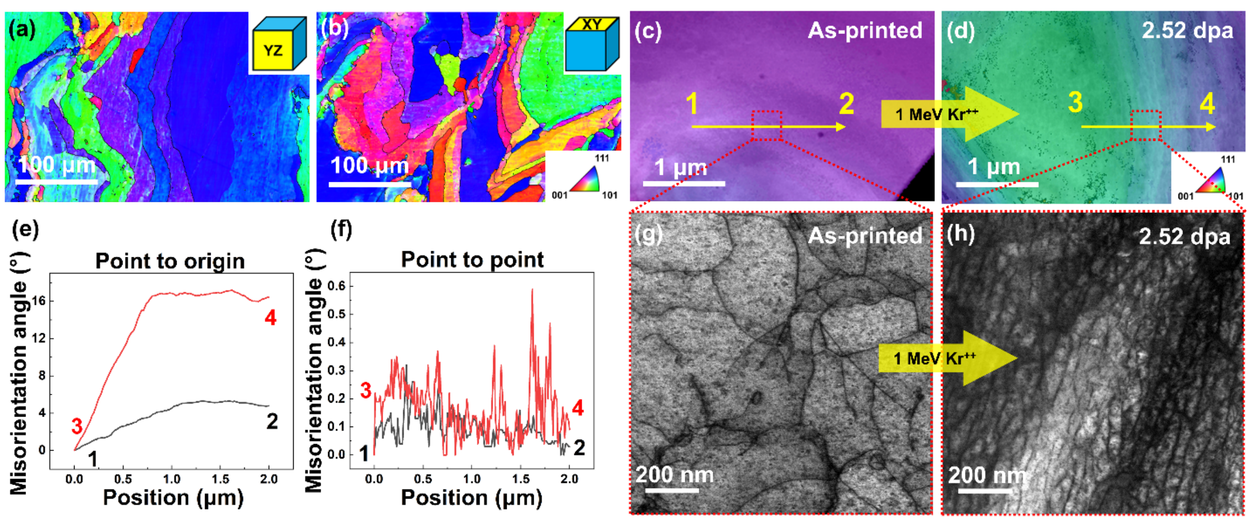

Figure 1. (a, b) SEM-EBSD IPF map of the YZ plane and XY plane of the LPBF-W. (c, d) TEM-ASTAR IPF map of the as-printed W and irradiated W sample. (e, f) Point to origin and point to point misorientation angle distribution of the yellow line in (c) and (d). (g, h) STEM-DF image of the red dash box area in (c) and (d) showing dislocation structures in unirradiated and irradiated conditions. After radiation, well-aligned dislocation loop rafts form.

Weak-beam dark-field (WBDF) TEM images in Fig. 2a-c show the progression of defect morphology with dose. At 0.36 dpa (Fig. 2a), the microstructure is dominated by small, discrete dislocation loops. As the dose increased to 1.08 dpa (Fig. 2b), loops began to align along parallel directions, forming loop rafts. At 2.52 dpa (Fig. 2c), larger, bright features appear, which are likely loop clusters, suggesting coalescence of individual loops at high damage levels. The quantitative evolution of loop number density and average loop diameter is plotted in Fig. 2d by counting over 50 loops in the same 100 nm × 100 nm region. Loop density increases sharply between 0.36 dpa and 0.72 dpa, followed by a significant decrease at higher doses beyond 1.80 dpa. In contrast, the average loop diameter remains stable (~2.8 nm) up to 2.16 dpa, after which it increases to ~3.4 nm and ultimately ~4.8 nm at 2.52 dpa. This inverse relationship between loop density and size suggests that beyond 1.80 dpa, the governing mechanism shifts from nucleation to loop coarsening and coalescence, leading to fewer but larger loops. Fig. 2e-g show the BF TEM images containing loop rafts indicated by yellow dotted circles. At 0.36 dpa (Fig. 2e), several short rafts are already visible, and their density increased markedly by 1.08 dpa and 2.52 dpa (Fig. 2f-g). The dynamic process of loop rafts formation can be found in Video S1. The evolution of average loop raft spacing is shown in Fig. 2h. A sharp reduction in spacing occurs between 0.36 dpa and 0.72 dpa, dropping from 55 to 37 nm, coinciding with the sharp rise in loop number density. Beyond this dose, the spacing stabilizes at approximately 30 nm. This trend indicates the saturation of loop raft formation at high dose levels, where spatial rearrangement dominates over further loop nucleation. The observed plateau in loop raft spacing at about 1.08 dpa (Fig. 2h), along with the gradual increase in loop number density between 0.72 and 1.08 dpa, suggests the onset of defect saturation. This behavior aligns with the dynamic equilibrium model proposed by Wang *et al*.[49], where a stable defect configuration emerges beyond 0.2 dpa, marked by constant loop and dislocation densities, reflecting a balance between defect generation and annihilation under continued irradiation.

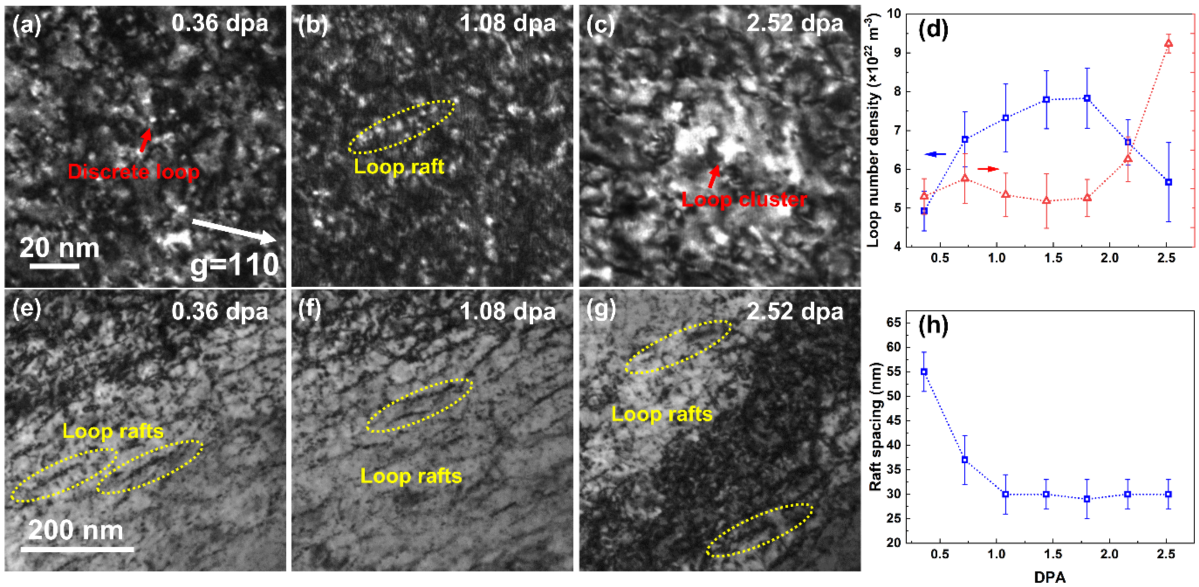

Figure 2. (a-c) Weak-beam dark-field TEM images in different dpa showing discrete dislocation loop in red arrows, loop rafts in yellow dotted circles, and loop clusters in red arrows. (d) The evolution of dislocation loop density and average loop diameter as a function of irradiation dose. (e-g) Bright field TEM images showing loop rafts at irradiation dose of 0.36 dpa, 1.08 dpa, and 2.52dpa. The loop rafts are shown in yellow dotted circles. (h) The evolution of loop raft spacing as a function of irradiation dose.

Fig. 3 presents STEM images of the same irradiated region acquired under three different diffraction vectors (g = [0$\bar{1}$1], [$\bar{2}$00], and [110]) to identify the Burgers vector of dislocation loops. In irradiated W, dislocation loops typically possess Burgers vectors of either <111> or <001> type [50, 51], corresponding to seven possible variants. The applied g vectors and the resulting g·b products for each Burgers vector variant are summarized in Table 1. The [0$\bar{1}$1] and [$\bar{2}$00] g vectors are taken under the [011] zone axis, while the [110] g vector is taken under [$\bar{1}$11] zone axis. According to the invisibility criterion, when g·b = 0, the dislocations are invisible. As shown in Fig. 3a and 3b, the same set of loop rafts (shown in yellow dotted circles) remains clearly visible under g = [0$\bar{1}$1] and g = [$\bar{2}$00] but becomes invisible under g = [110] (Fig. 3c). This contrast behavior indicates that the loops have a common Burgers vector of **b** = $[1\bar{1}1]$, for which g·b = 0 under g = [110] but nonzero under the other two conditions. Moreover, most loop rafts are consistently aligned along the <110> crystallographic direction, which is perpendicular to the Burgers vector. The rafting direction may also be influenced by thin foil thickness (i.e. alignment along a local thickness gradient toward the foil edge [52]). Notably, in Fig. 3c, raft segments with other orientations are also observed (some of them are circled in red), indicating that multiple rafting directions can coexist within the same grain [53]. The formation of those directional dislocation loop rafts in irradiated LPBF-W is largely driven by elastic interactions among glissile interstitial loops with similar Burgers vectors. As these loops migrate, they tend to align along a common direction due to mutual repulsion and minimize elastic energy by forming low energy configurations. In addition, prior studies have shown that mobile interstitial clusters can undergo self-trapping into less mobile configurations [54]. Mobile interstitial point defects may flow in and be preferentially trapped in the tensile region of an interstitial loop to form smaller interstitial clusters, which can subsequently interact elastically with the loop and participate in the rafting process. The loop raft characteristic is similar to the traditionally processed W.

Table 1. g·b values for various g vectors used for analysis and the seven possible Burgers vectors of the dislocation loops in Kr irradiated W in this work.

b\g	g = $[0\bar{1}1]$	g = $[\bar{2}00]$	g = [110]
[111]	0	-2	2
$[\bar{1}11]$	0	2	0
$[1\bar{1}1]$	2	-2	0
$[11\bar{1}]$	-2	-2	2
[001]	1	0	0
[010]	-1	0	1
[100]	0	-2	1

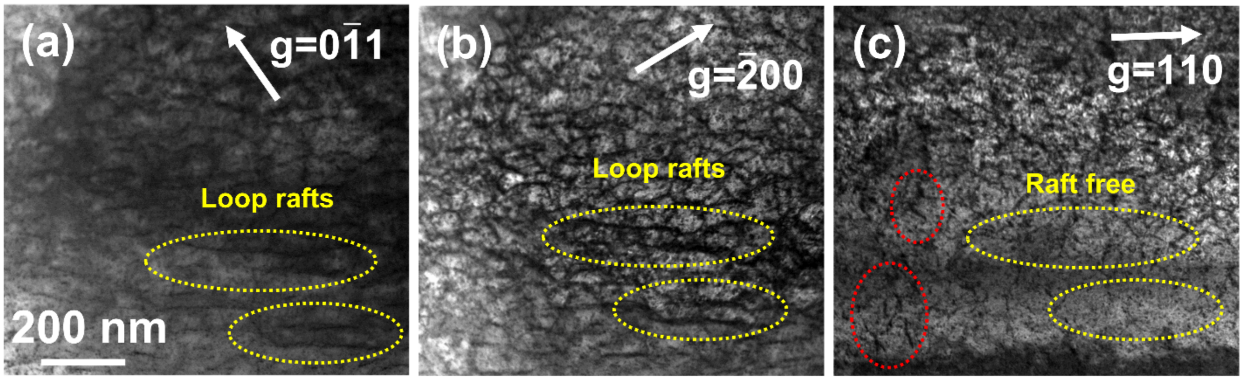

Figure 3. Burgers vector analysis of dislocation loops in the rafts. (a) STEM image of the same area under [0$\bar{1}$1] g vector. (b) STEM image of the same area under [$\bar{2}$00] g vector. (c) STEM image of the same area under [110] g vector. Loop rafts are shown in yellow and red dotted circles.

An intriguing feature of LPBF-W is the presence of dispersed oxide nanoparticles, which serve as natural second-phase defect sinks. Fig. 4a shows a series of *in situ* snapshots capturing the behavior of an interstitial loop (red arrow) interacting with a W/WO_3 phase boundary (marked by yellow dotted line). Between 0.74 and 0.76 dpa, the loop gradually dissolved into the interface over ~13 seconds, suggesting that interstitial clusters can migrate, redistribute and be gradually absorbed at the oxide boundary within this timeframe. Video S2 shows the dynamic process of loop absorption. The detailed mechanism is to be discussed. This dynamic absorption highlights the potential of such interfaces to act as effective defect sinks. Fig. 4b and 4c reveal the spatial distribution of loop rafts around oxide particles at 0.72 and 2.52 dpa, respectively. Local specimen thickness can significantly affect defect evolution in TEM foils because the two free surfaces act as sinks for point defects [49, 55]. As shown in Fig. 4b, the raft density is lower in the lower-left region but higher in the upper-right region. This trend can be attributed to enhanced surface sink effects in the thinner region, where a larger fraction of dislocation loops is removed from the free surfaces, thereby suppressing loop accumulation and raft development. Thickness measurement

(Fig. S6) has been performed around one of the particles to rule out the effect of the film thickness variation on the dislocation contrast. The region showing dislocation loop-precipitate interaction has an average thickness of 67 nm, as shown in Fig. S6. A distinct raft denuded zone, approximately 35 nm in radius, is observed surrounding the oxide particle at 0.72 dpa, while loop rafts are dense in the surrounding matrix. At 2.52 dpa, this depletion zone contracts to ~25 nm, likely due to the higher defect flux overwhelming the sink efficiency of the interface.

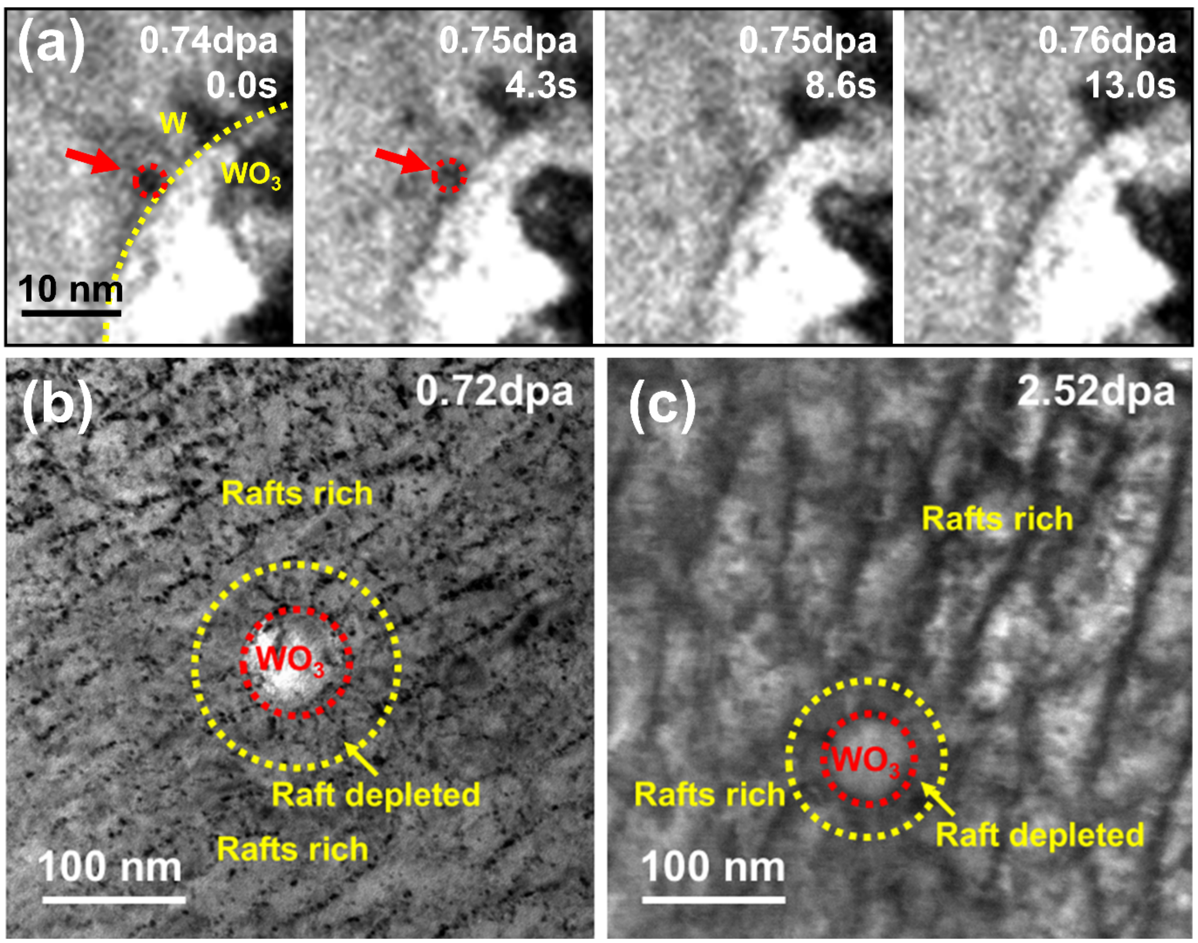

Figure 4. (a) Representative *in situ* video snapshots illustrating the absorption of dislocation loops into the W/WO_3 phase boundary. Yellow dash line shows the W/WO_3 phase boundary, red arrow shows an interstitial loop along the phase boundary. Video can be found in supplementary video S2 (b) Bright field TEM image under 0.72 dpa showing the WO_3 particle breaks the loop rafts

forming raft depleted area near the particle. (c) Bright field TEM image under 2.52 dpa. Higher irradiation dose results in much longer loop rafts, which are interrupted by WO_3 particle, forming a smaller raft depleted area.

Fig. 5a-c show the HRTEM image of a WO_3 particle and the surrounding W matrix after radiation. Despite the reduced oxygen content, the FFT result in Fig. 5b confirms that the core of the particle retains the monoclinic WO_3 structure. The orientation relationship based on the FFT result can be summarized as: $[11\bar{3}]$ WO_3 // $[\bar{1}11]$ W, (211) WO_3 // (110) W.

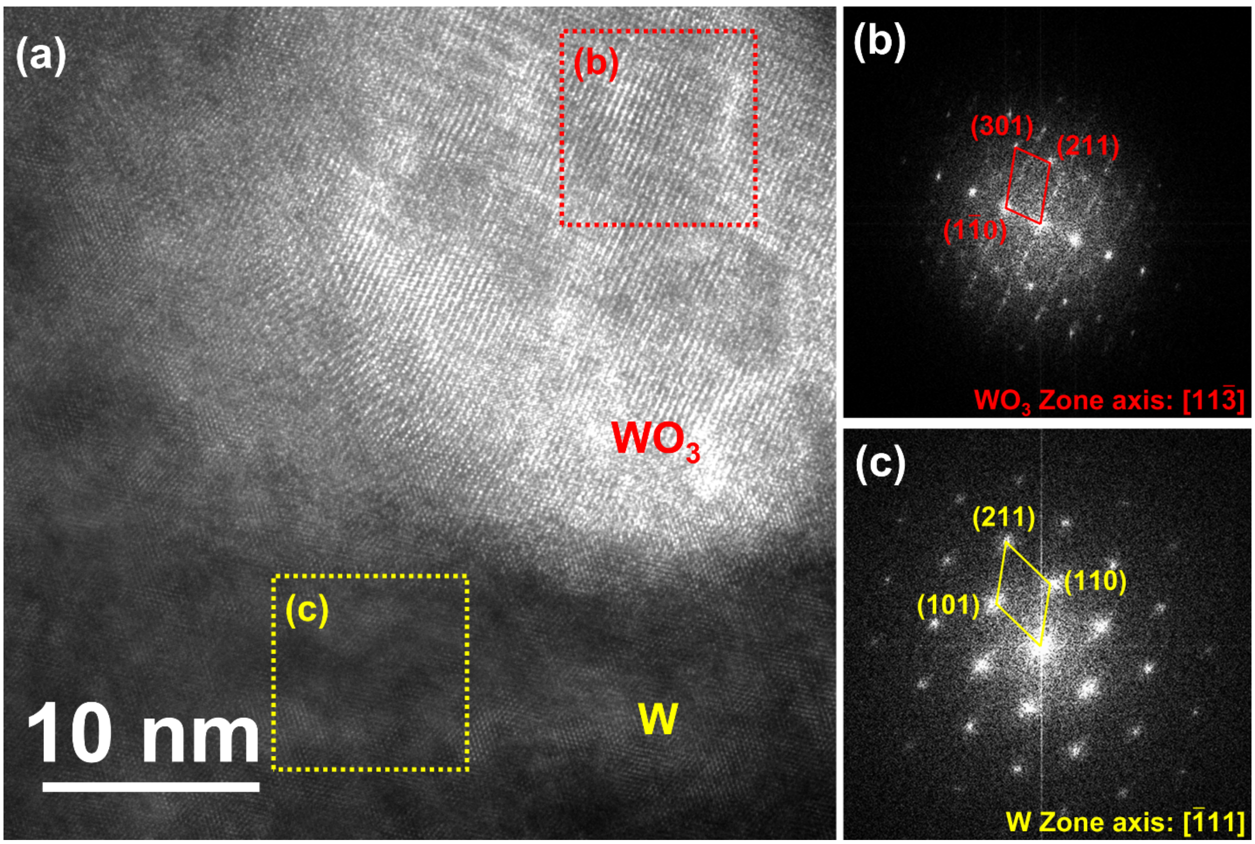

Figure 5. (a) HRTEM image of a WO_3 nanoparticle and the surrounding W matrix. (b) Fast Fourier transform (FFT) of the center of the particle area in red dash box in (a). (c) FFT of the W matrix area in yellow dash box in (a).

According to prior studies, heterogeneous phase interfaces preferentially absorb interstitial defects, resulting in surrounding regions enriched in vacancies [26]. In this work, direct *in situ* evidence of dislocation loop dissociation at the W/WO_3 phase boundary is captured in Fig. 4a, indicating that the interface acts as an efficient sink for irradiation-induced interstitial loops. Under the irradiation temperature used in this study (i.e., 400 °C), vacancies have sufficient mobility to diffuse over moderate distances [56, 57]. Shang *et al.* [58] proposed that spontaneous recombination between the interstitial and vacancy type Frank loops can occur at coherent twin boundaries. Similarly, we suggest that the W/WO_3 interfaces may also absorb the vacancies that promote local recombination at the interface, leading to the observed disappearance of interstitial loops over time, as shown in the *in situ* snapshots (Fig. 4a). Hence, the W/WO_3 interface can act as a dynamic recombination site, contributing to localized defect depletion and microstructural stabilization under irradiation.

4. Conclusions

In situ heavy ion irradiation was conducted on a LPBF-W with oxide nanoparticles at 400 °C to 2.52 dpa. This is the first study to report the radiation behavior of W made by LPBF. Compared to conventionally processed W, LPBF-W exhibits similar dislocation loop behavior, including the formation of aligned loop rafts with ~30 nm spacing and identical Burgers vectors. Notably, these loop rafts induce significant lattice distortion, leading to gradual grain misorientation up to 17°, which may represent an incipient stage of grain refinement, a phenomenon rarely reported in previous work. Distinctively, LPBF-W includes tungsten oxide nanoparticles with a volume fraction of ~0.13% acting as defect sinks. These particles disrupt the surrounding loop rafts and create localized raft depleted zones. In future studies, the deliberate incorporation of similar precipitates network with reduced spacing via LPBF may provide an effective pathway to enhance high-dose irradiation tolerance in W-based materials, given the inherent flexibility of additive manufacturing in compositional and microstructural design.

Acknowledgments:

We would like to acknowledge the financial support from DOE Fusion Energy Sciences (FES) under grant number DE-SC0024583. Yu and Graening acknowledge support of the DOE FES Fusion Materials program at the Oak Ridge National Laboratory (ORNL). ORNL is operated by UT-Battelle, LLC un-der Contract No. DE-AC05-00OR22725 for the U.S. Department of Energy. The United States (US) Government retains and the publisher, by accepting the article for publication, acknowledges that the US Government retains a non-exclusive, paid-up, irrevocable, world-wide license to publish or reproduce the published form of this manuscript, or allow others to do so, for US Government purposes. The DOE will provide public access to these results of federally sponsored research in accordance with the DOE Public Access Plan (http://energy.gov/downloads/doe-public-access-plan). We also thank Peter M. Baldo and Edward A. Ryan at Argonne National Laboratory for their help during *in situ* radiation experiments. The IVEM facility at Argonne National Laboratory is supported by DOE-Office of Nuclear Energy. Accesses to the Microscopy Centers at Purdue University and the DoE Center for Integrated Nanotechnologies managed by Los Alamos National Laboratory is also acknowledged.

References

[1] V. Philipps, Tungsten as material for plasma-facing components in fusion devices, Journal of nuclear materials 415(1) (2011) S2-S9.
[2] J. Roth, E. Tsitrone, A. Loarte, T. Loarer, G. Counsell, R. Neu, V. Philipps, S. Brezinsek, M. Lehnen, P. Coad, Recent analysis of key plasma wall interactions issues for ITER, Journal of nuclear materials 390 (2009) 1-9.
[3] H. Bolt, V. Barabash, W. Krauss, J. Linke, R. Neu, S. Suzuki, N. Yoshida, A.U. Team, Materials for the plasma-facing components of fusion reactors, Journal of nuclear materials 329 (2004) 66-73.
[4] M. Kaufmann, R. Neu, Tungsten as first wall material in fusion devices, Fusion Engineering and Design 82(5-14) (2007) 521-527.
[5] M. Liang, F. Xie, J. Song, Advances in research on helium ion irradiation in tungsten-based plasma-facing materials, Materials Today Communications (2025) 112002.
[6] S.J. Zinkle, J.T. Busby, Structural materials for fission & fusion energy, Materials today 12(11) (2009) 12-19.
[7] Y. Li, L. Wang, G. Ran, Y. Yuan, L. Wu, X. Liu, X. Qiu, Z. Sun, Y. Ding, Q. Han, X. Wu, H. Deng, X. Huang, In-situ TEM investigation of 30 keV he+ irradiated tungsten: Effects of temperature, fluence, and sample thickness on dislocation loop evolution, Acta Materialia 206 (2021).
[8] X. Hu, T. Koyanagi, M. Fukuda, N.A.P.K. Kumar, L.L. Snead, B.D. Wirth, Y. Katoh, Irradiation hardening of pure tungsten exposed to neutron irradiation, Journal of Nuclear Materials 480 (2016) 235-243.
[9] G.L. Kulcinski, J. Laidler, D. Doran, Simulation of high fluence fast neutron damage with heavy ion bombardment, Radiation Effects 7(3-4) (1971) 195-202.
[10] Y. Zheng, Y. Zuo, D. Yuan, D. Zhou, Y. Xu, P. Fan, J. Zhu, Z. Wang, S. Zhu, Investigation of Radiation Damage in Stainless steel, Tungsten and Tantalum by Heavy Ion Irradiations, Nuclear Physics A 834(1-4) (2010) 761c-763c.
[11] R. Nelson, D. Mazey, J. Hudson, The use of ion accelerators to simulate fast neutron-induced voidage in metals, Journal of Nuclear Materials 37(1) (1970) 1-12.
[12] F. Häussermann, ANALYSIS OF DISLOCATION LOOPS IN TUNGSTEN PRODUCED BY 60 keV ION IRRADIATION, Max-Planck-Institut fuer Metallforschung, Stuttgart, 1972.
[13] F. Häussermann, STUDY OF THE RADIATION DAMAGE PRODUCED BY ENERGETIC GOLD IONS IN MOLYBDENUM AND TUNGSTEN, Max-Planck-Institut fuer Metallforschung, Stuttgart, 1972.
[14] F. Häussermann, M. Rühle, M. Wilkens, Black-white contrast figures from small dislocation loops II. Application of the first order solution to small loops in ion-irradiated tungsten foils, physica status solidi (b) 50(2) (1972) 445-457.
[15] X. Yi, M.L. Jenkins, K. Hattar, P.D. Edmondson, S.G. Roberts, Characterisation of radiation damage in W and W-based alloys from 2 MeV self-ion near-bulk implantations, Acta Materialia 92 (2015) 163-177.
[16] X. Yi, M.L. Jenkins, M.A. Kirk, Z. Zhou, S.G. Roberts, In-situ TEM studies of 150 keV W+ ion irradiated W and W-alloys: Damage production and microstructural evolution, Acta Materialia 112 (2016) 105-120.
[17] X. Yi, M. Jenkins, M. Briceno, S. Roberts, Z. Zhou, M. Kirk, In situ study of self-ion irradiation damage in W and W–5Re at 500 C, Philosophical Magazine 93(14) (2013) 1715-

1738.
[18] B. Eyre, R. Bullough, On the formation of interstitial loops in bcc metals, Philosophical Magazine 12(115) (1965) 31-39.
[19] Ł. Ciupiński, O.V. Ogorodnikova, T. Płociński, M. Andrzejczuk, M. Rasiński, M. Mayer, K.J. Kurzydłowski, TEM observations of radiation damage in tungsten irradiated by 20MeV W ions, Nuclear Instruments and Methods in Physics Research Section B: Beam Interactions with Materials and Atoms 317 (2013) 159-164.
[20] Z. Zhang, K. Yabuuchi, A. Kimura, Defect distribution in ion-irradiated pure tungsten at different temperatures, Journal of Nuclear Materials 480 (2016) 207-215.
[21] V. Sikka, J. Moteff, ``Rafting''in neutron irradiated tungsten, Journal of Nuclear Materials 46(2) (1973) 217-219.
[22] M. Wen, N.M. Ghoniem*, B.N. Singh, Dislocation decoration and raft formation in irradiated materials, Philosophical Magazine 85(22) (2005) 2561-2580.
[23] S.L. Dudarev, K. Arakawa, X. Yi, Z. Yao, M.L. Jenkins, M.R. Gilbert, P.M. Derlet, Spatial ordering of nano-dislocation loops in ion-irradiated materials, Journal of Nuclear Materials 455(1-3) (2014) 16-20.
[24] O. El-Atwani, E. Aydogan, E. Esquivel, M. Efe, Y.Q. Wang, S.A. Maloy, Detailed transmission electron microscopy study on the mechanism of dislocation loop rafting in tungsten, Acta Materialia 147 (2018) 277-283.
[25] O. El-Atwani, N. Li, M. Li, A. Devaraj, J.K.S. Baldwin, M.M. Schneider, D. Sobieraj, J.S. Wróbel, D. Nguyen-Manh, S.A. Maloy, Outstanding radiation resistance of tungsten-based high-entropy alloys, Science advances 5(3) (2019) eaav2002.
[26] I.J. Beyerlein, M.J. Demkowicz, A. Misra, B.P. Uberuaga, Defect-interface interactions, Progress in Materials Science 74 (2015) 125-210.
[27] J. Li, K.Y. Yu, Y. Chen, M. Song, H. Wang, M.A. Kirk, M. Li, X. Zhang, In situ study of defect migration kinetics and self-healing of twin boundaries in heavy ion irradiated nanotwinned metals, Nano Lett 15(5) (2015) 2922-7.
[28] K.Y. Yu, Y. Chen, J. Li, Y. Liu, H. Wang, M.A. Kirk, M. Li, X. Zhang, Measurement of Heavy Ion Irradiation Induced In-Plane Strain in Patterned Face-Centered-Cubic Metal Films: An in Situ Study, Nano Lett 16(12) (2016) 7481-7489.
[29] S. Stangebye, K. Ding, Y. Zhang, E. Lang, K. Hattar, T. Zhu, J. Kacher, O. Pierron, Direct Observation of Grain-Boundary-Migration-Assisted Radiation Damage Healing in Ultrafine Grained Gold under Mechanical Stress, Nano Lett 23(8) (2023) 3282-3290.
[30] O. El-Atwani, W.S. Cunningham, E. Esquivel, M. Li, J.R. Trelewicz, B.P. Uberuaga, S.A. Maloy, In-situ irradiation tolerance investigation of high strength ultrafine tungsten-titanium carbide alloy, Acta Materialia 164 (2019) 547-559.
[31] M.J. Zhuo, E.G. Fu, L. Yan, Y.Q. Wang, Y.Y. Zhang, R.M. Dickerson, B.P. Uberuaga, A. Misra, M. Nastasi, Q.X. Jia, Interface-enhanced defect absorption between epitaxial anatase TiO2 film and single crystal SrTiO3, Scripta Materialia 65(9) (2011) 807-810.
[32] X. Wang, Q. Yang, W. Wu, W. Zhang, Y. Zhang, D. Yan, K. Gan, B. Liu, Z. Li, Excellent radiation resistance via enforced local non-directional He diffusion in a WTaCrV multicomponent alloy containing coherent ordered nanoprecipitates, Acta Materialia 282 (2025).
[33] E. Lang, X. Wang, R. Kolasinski, J.P. Allain, Dispersion-strengthened tungsten alloy composites, Fusion Energy Technology R&D Priorities2025, pp. 65-69.
[34] M. Rieth, R. Doerner, A. Hasegawa, Y. Ueda, M. Wirtz, Behavior of tungsten under irradiation and plasma interaction, Journal of Nuclear Materials 519 (2019) 334-368.

[35] S.-H. Pan, G.-C. Yao, Y.-N. Cui, F.-S. Meng, C. Luo, T.-Q. Zheng, G. Singh, Additive manufacturing of tungsten, tungsten-based alloys, and tungsten matrix composites, Tungsten 5(1) (2022) 1-31.
[36] A. Iveković, N. Omidvari, B. Vrancken, K. Lietaert, L. Thijs, K. Vanmeensel, J. Vleugels, J.-P. Kruth, Selective laser melting of tungsten and tungsten alloys, International Journal of Refractory Metals and Hard Materials 72 (2018) 27-32.
[37] K. Li, D. Wang, L. Xing, Y. Wang, C. Yu, J. Chen, T. Zhang, J. Ma, W. Liu, Z. Shen, Crack suppression in additively manufactured tungsten by introducing secondary-phase nanoparticles into the matrix, International Journal of Refractory Metals and Hard Materials 79 (2019) 158-163.
[38] T. Yamamoto, M. Hara, Y. Hatano, Effects of fabrication conditions on the microstructure, pore characteristics and gas retention of pure tungsten prepared by laser powder bed fusion, International Journal of Refractory Metals and Hard Materials 95 (2021).
[39] D. Wang, Z. Wang, K. Li, J. Ma, W. Liu, Z. Shen, Cracking in laser additively manufactured W: Initiation mechanism and a suppression approach by alloying, Materials & Design 162 (2019) 384-393.
[40] G. Wang, H. Ouyang, C. Fan, Q. Guo, Z. Li, W. Yan, Z. Li, The origin of high-density dislocations in additively manufactured metals, Materials Research Letters 8(8) (2020) 283-290.
[41] D. Hu, N. Grilli, W. Yan, Dislocation structures formation induced by thermal stress in additive manufacturing: Multiscale crystal plasticity modeling of dislocation transport, Journal of the Mechanics and Physics of Solids 173 (2023).
[42] J.-H. Lin, Y.-T. Yan, J.-L. Qi, C.-Y. Zha, Atomic tailoring-induced deficiency in tungsten oxides for high-performance energy-related devices, Tungsten 6(2) (2023) 269-277.
[43] M. Gillet, K. Mašek, E. Gillet, Structure of tungsten oxide nanoclusters, Surface Science 566-568 (2004) 383-389.
[44] H. Sheng, Z. Sun, I. Uytdenhouwen, G. Van Oost, J. Vleugels, Temperature and deformation effect on the low and high angle grain boundary structure of a double forged pure tungsten, International Journal of Refractory Metals and Hard Materials 50 (2015) 184-190.
[45] O. El Atwani, H.T. Vo, M.A. Tunes, C. Lee, A. Alvarado, N. Krienke, J.D. Poplawsky, A.A. Kohnert, J. Gigax, W.Y. Chen, M. Li, Y.Q. Wang, J.S. Wróbel, D. Nguyen-Manh, J.K.S. Baldwin, O.U. Tukac, E. Aydogan, S. Fensin, E. Martinez, A quinary WTaCrVHf nanocrystalline refractory high-entropy alloy withholding extreme irradiation environments, Nature Communications 14(1) (2023) 2516.
[46] D. Kaoumi, A. Motta, R. Birtcher, A thermal spike model of grain growth under irradiation, Journal of Applied Physics 104(7) (2008).
[47] H. Gietl, T. Koyanagi, X. Hu, M. Fukuda, A. Hasegawa, Y. Katoh, Neutron irradiation-enhanced grain growth in tungsten and tungsten alloys, Journal of Alloys and Compounds 901 (2022).
[48] N. Nita, R. Schaeublin, M. Victoria, Impact of irradiation on the microstructure of nanocrystalline materials, Journal of Nuclear Materials 329-333 (2004) 953-957.
[49] S. Wang, W. Guo, T. Schwarz-Selinger, Y. Yuan, L. Ge, L. Cheng, X. Zhang, X. Cao, E. Fu, G.-H. Lu, Dynamic equilibrium of displacement damage defects in heavy-ion irradiated tungsten, Acta Materialia 244 (2023).
[50] W. Setyawan, G. Nandipati, K.J. Roche, H.L. Heinisch, B.D. Wirth, R.J. Kurtz, Displacement cascades and defects annealing in tungsten, Part I: Defect database from molecular dynamics simulations, Journal of Nuclear Materials 462 (2015) 329-337.

[51] A.E. Sand, S. Dudarev, K. Nordlund, High-energy collision cascades in tungsten: Dislocation loops structure and clustering scaling laws, Europhysics Letters 103(4) (2013) 46003.
[52] M. Hernández-Mayoral, Z. Yao, M.L. Jenkins, M.A. Kirk, Heavy-ion irradiations of Fe and Fe–Cr model alloys Part 2: Damage evolution in thin-foils at higher doses, Philosophical Magazine 88(21) (2008) 2881-2897.
[53] S.J. Zinkle, B.N. Singh, Microstructure of neutron-irradiated iron before and after tensile deformation, Journal of Nuclear Materials 351(1-3) (2006) 269-284.
[54] D.A. Terentyev, T.P. Klaver, P. Olsson, M.C. Marinica, F. Willaime, C. Domain, L. Malerba, Self-trapped interstitial-type defects in iron, Phys Rev Lett 100(14) (2008) 145503.
[55] R.-Y. Zheng, W.-Z. Han, Comparative study of radiation defects in ion irradiated bulk and thin-foil tungsten, Acta Materialia 186 (2020) 162-171.
[56] A. Založnik, D. Dellasega, G. Alberti, M. Passoni, T. Schwarz-Selinger, M.I. Patino, M.J. Simmonds, M.J. Baldwin, G.R. Tynan, Effect of grain size on defect annealing in displacement-damaged tungsten, Nuclear Materials and Energy 39 (2024).
[57] R. Ramachandran, S. Balaji, Study of irradiation-induced vacancy-type defects in tungsten using positron annihilation spectroscopy, Nuclear Materials and Energy 37 (2023).
[58] Z. Shang, T. Niu, T. Sun, S. Xue, C. Fan, W.-Y. Chen, M. Li, H. Wang, X. Zhang, In situ study on radiation response of a nanotwinned steel, Scripta Materialia 220 (2022).